185

Design of a Mathematical Computational Phantom for Oncopediatric Patients for the Pet/Ct Study

Manuel I. León-Madrid[1], Georgina C. Waldo[1], Karen A. Castañeda[1], Pablo V. Cerón[2] and Modesto A. Sosa[1*]

[1]Department of Physical Engineering, DCI, University of Guanajuato, 37150 Leon, Gto., Mexico.

[2]Department of Environmental Sciences, DCIT, University of Quintana Roo, 77019, Chetumal, QRoo, Mexico.

Abstract: The main objective of this work was to design a mathematical computational phantom for on-pediatric patients, incorporating the main organs for 18F-FDG absorption rates. The organs were located within the body using CT and ultrasound images, while the body was constructed using anthropometric information from the Latin American population as a reference. The absorption of 18F-FDG in each organ was determined during PET/CT exploration of the entire body. The number of photons emitted by the organs was calculated using their respective metabolic absorption rate values. The absorbed dose was estimated using Monte Carlo N-particle (MCNP) for three different activities: 6.6 mCi, 11 mCi, and 13 mCi, to compare the results with previously reported research. The tissues that absorbed the largest doses were the brain, heart, and bladder. The absorbed dose in the brain was 14.34 mGy, 23.90 mGy, and 26.07 mGy, respectively. In the heart, it was 14.97 mGy, 24.95 mGy, and 27.22 mGy, respectively. The bladder, on the other hand, was the organ that presented the largest absorbed dose, with 24.62 mGy, 41.03 mGy, and 44.76 mGy, respectively. The other organs studied: the eye lens, gonads, lungs, kidneys, thyroid, and uterus, showed an average dose much lower, approximately 5 mGy.

Keywords: PET/CT scan, MCNP5, Pediatric Computational Phantom, 18F-FDG, Absorbed dose.

1 Introduction

According to the World Health Organization (WHO) [1], cancer is one of the main diseases affecting children and teenagers worldwide. Every year, over 400,000 children between the ages of 0 and 19 are diagnosed with cancer. Childhood cancer is difficult to prevent or detect through screening before relevant symptoms appear as it has no clear cause beyond genetics. The main types of childhood cancer include leukemias, brain cancer, lymphomas, and solid tumors such as neuroblastomas and Wilms tumors[2]. In Latin America alone, around 30,000 children are expected to be diagnosed with cancer, and 33% will die due to it. Several reasons for the low success rate in treating childhood cancer include delayed diagnosis, inaccurate diagnosis, inaccessible therapy, abandonment of treatment, intoxication as a side effect, and avoidable relapse.

Additionally, several studies have found that anthropometric measurements of pediatric patients differ between some regions of the world due to the existence of many ethnic groups and their corresponding body mass indexes, waist-hip ratio, and waist-to-height ratio, directly related to genetic, environmental, and nutritional factors

[3]. In some countries of Latin America, such as Mexico, for instance, obesity in 6-year-old children corresponds to 24.3%, and for 12-year-old children, it's at 32.5% during this infancy period [4], which modifies anthropometry. Therefore, there are particularities in the size and body density in this population. As a result, a higher quantity of contrast media in nonmature tissues in radiological studies is needed in children of larger sizes. Given this background, estimating the absorbed dose in organs of 12-year-old pediatric patients due to the absorption of [18F] Fluorodeoxyglucose (18F-FDG) during a positron emission tomography (PET/CT) study is considered worthwhile.

To achieve an accurate clinical evaluation and diagnosis, the use of special equipment is required, which is where PET/CT scanning techniques come in. Although 18-FDG is one of the most used radiopharmaceuticals in PET/CT procedures, it is not optimal due to its lack of specificity for cancer cells. Glucose is metabolized in various tissues, including the heart, lungs, bladder, brain, and muscles, and has maximum uptake during inflammatory lesions. This fact highlights a new need in the early diagnosis of cancer, which is to establish a dose control procedure throughout

---

* Corresponding author e-mail: modesto@fisica.ugto.mx

diagnosis and treatment.

One way to estimate the dose contribution is by applying dosimetry techniques such as patient and phantom measurements or computer simulation. The international community widely accepts the use of computational tools such as mathematical phantoms [5,6]. These types of phantoms enable the estimation of dosimetric quantities such as absorbed dose, equivalent dose, particle flow, and their energy distribution without the need to irradiate a patient or have measuring instruments such as ionization chambers or Geiger counters [6]. Nowadays, the most popular computational phantoms are those based on voxels, which allow achieving a phantom that is almost identical to that of the patient. However, this requires more computational processing, and the results can be significantly different from traditional mathematical phantoms such as the ORNL family, which is based on simple mathematical elements such as spheres, ellipsoids, squares, and cylinders as the main representation of the human body and its organs [7,8].

To estimate the absorbed dose in radiosensitive and high glucose-consuming organs, various techniques have been reported by research groups around the world using different measurements and reference values [9]. Alkhorayef reported an effective dose related to the application of 18F-FDG of 12.1 ± 4 mSv (5.0-20.4) [10]. Similarly, Quinn et al. reported absorbed dose values between 4 and 46 mGy [11], depending on the organ and the patient's age, using commercial dose-care software and PMMA phantoms. In contrast, Mohammadi and Akhlaghi [12] employed mathematical phantoms, UF and IT'IS, with ICRP data to report an absorbed dose range due to 18F contribution from 2 mGy to 40 mGy.

This work aims to provide a simple methodology that utilizes MCNP5 and macro bodies to design a 12-year hybrid phantom containing the main organs related to the 18F-FDG uptake rate. CT and ultrasound images, along with anatomical references, were used to locate the organs within the body, while anthropometric information was used as a reference for constructing the body box [13].

2 Experimental Section

2.1 Design and Construction of the Phantom Shell

A BOMAB geometry served as the foundation for the phantom shell design. Anthropomorphic parameters, including height, eye height, transverse diameter, and anteroposterior (AP) dimensions of the thorax, neck, head, and interpupillary distance, were derived from a 12-year-old population for the dimensions of the phantom, see Fig 1. The parameters utilized for the design of the phantom shell were:

- Height
- Height to waist
- Chest´s depth
- Chest's width
- Neck's width
- Neck's height
- Head's height
- Head's wight
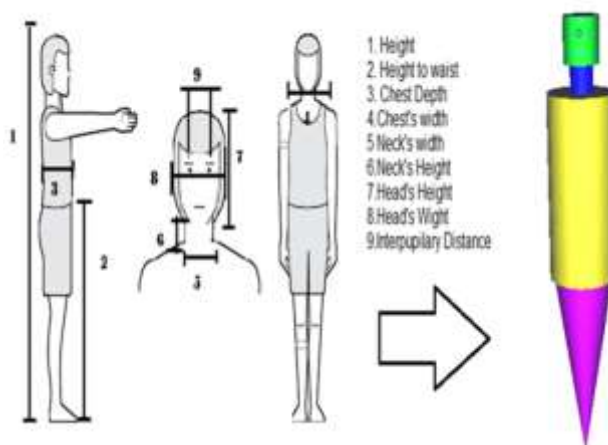- Interpupillary Distance

Fig. 1: Landmarks employed in phantom's shell

Given that the measurements were based on average values, adjustments in height and weight could be considered as customization factors for future reference.

To utilize this type of phantom effectively, it is imperative to establish a suitable coordinate system as a reference. The origin (0,0,0) was positioned at the base of the trunk, with the z-axis aligned in the cranial-caudal direction, the x-axis in the lateral (left-right) orientation, and the y-axis in the anteroposterior direction (back to front)

2.2 Modeling and Location of the Radiosensitive Organs

The selection of organs of interest was based on the IAEA list of radiosensitive organs[14], as well as studies by Huang et al [15,16], Gelfand [17], and Lee et al [18]. Criteria for selection included the nature of the organ, its metabolic consumption of glucose, and the elimination process of the radiopharmaceutical. The chosen organs comprised the brain, eye lens, thyroid, lung, heart, kidney, bladder, uterus, and gonads.

Following the selection of organs, the modeling and parameterization process commenced. The most suitable types of geometry and macrobodies were determined for constructing each organ. Medical images, obtained from

computed tomography, ultrasound, and magnetic resonance imaging, were analyzed using various software tools such as Radiant, ImageJ, RadView, and Python. These software tools facilitated the extraction of width, length, height, and center of mass data for each organ from pediatric patients within the specified age range (11-13 years old), as depicted in Figure 2.
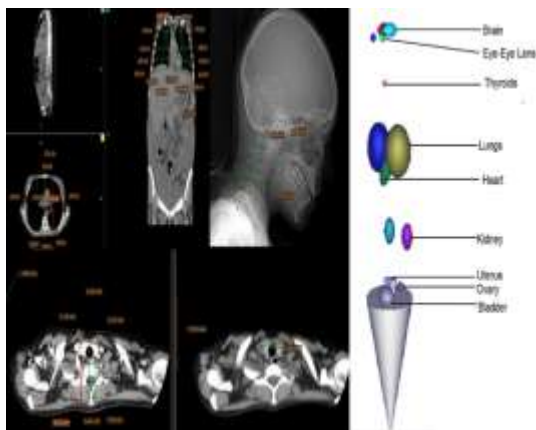

Fig. 2: Organ's modeling and placement.

Supplementary data were sourced from the Radiology Assistant website repository [19], as detailed in Table 1.

Table 1. Organ Parameterization Details.

Organ of interest	Macrobody	Parameters used
Heart	Ellipsoid	A-T, C-C and T diameters
Brain lobes	Ellipsoid	A-T, C-C and T diameters
Thyroid lobes	Ellipsoid	A-T, C-C and T diameters
Eye/lens	Sphere	Eye diameter
Lungs	Ellipsoid	A-T, C-C and T diameters
Kidneys	Ellipsoid	A-T, C-C and T diameters
Bladder	Ellipsoid	A-T, C-C and T diameters
Uterus	Truncated cone	Top radius, bottom radius and height
Ovaries	Ellipsoid	A-T, C-C and T diameters
Testicles	Ellipsoid	A-T, C-C and T diameters

Subsequently, anatomical landmarks such as the axis of the pubic symphysis, the positions of vertebrae C7, T1, T12, L1, the sacrum, and the thoracic diameter were utilized for organ placement. These references also facilitated the determination of lengths for the macrobodies representing the torso, neck, head, legs, and eyes [13]. Using these measurements, the coordinates of the organs in xyz were computed by standardizing them with respect to the corresponding landmarks (refer to Table 2).

Table 2. Body Parameterization Details.

Anatomical structure	Macrobody	X-axis reference	Y-axis reference	Z-axis reference
Torso	Elliptical cylinder (REC)	Thoracic transverse diameter	Chest thickness	Pubic-shoulder height
Neck	Circular cylinder	Neck width	NA	Neck height
Head	Circular cylinder	Head width	A-P diameter	Head height
Legs	Truncated cone	Thigh width (top cap) Ankle width (bottom cap)	NA	Waist-ankle height
Eyes	Spheres	Interpupillary distance	Eye radius	Eye height

Upon computing the dimensions and centers of mass, the organs were positioned within the phantom shell, and the elemental composition was integrated into the MCNP code. The elemental composition data were sourced from the GEANT4-GATE and IAEA libraries [20,21] (see Table 3).

2.3 MCNP Source Card

Although the annihilation process is commonly assumed to be monoenergetic, researchers such as Shibuya et al [22]. have demonstrated that there is an energy spectrum associated with it. For this study, the energy spectrum reported by Shibuya was incorporated into the MCNP code and utilized as the source card (refer to Figure 3).

To estimate the number of photons emitted in a PET/CT study, the following equation was employed:

$$N = 3.7 \times 10^7 * A * \lambda * 2 \qquad (1)$$

Here, N represents the number of photons emitted due to annihilation, and A is the 18F-FDG activity in mCi. After computing the total number of photons, this value was multiplied by the 18F-FDG absorption fractions reported by Mejia et al [23]. to determine the radiopharmaceutical absorption percentage for 18F-FDG in each organ, as illustrated in Table 4.

Table 3. Organ Density and Elemental Composition.

Tissue	Density (gr/cm3)	Elemental Composition (%)									
		H	C	N	O	Na	P	S	Cl	K	Ca
Brain	1.04	10.7	14.5	2.2	71.2	0.2	0.4	0.2	0.3	0.3	
Heart	1.05	10.4	13.9	2.9	71.8	0.1	0.2	0.2	0.2	0.3	
Eye	1.07	9.6	19.5	5.7	64.6	0.1	0.1	0.3	0.1	0	
Ovaries	1.05	10.5	9.3	2.4	76.8	0.2	0.2	0.2	0.2	0.2	
Lung	0.26	0.103	0.105	0.031	0.749	0.002	0.002	0.003	0.003	0.002	
Kidney	1.05	10.3	13.2	3	72.4	0.2	0.2	0.2	0.2	0.2	0.001
Testicles	1.04	10.6	9.9	2	76.6	0.2	0.1	0.2	0.2	0.2	
Thyroid	1.05	10.4	11.9	2.4	74.5	0.2	0.1	0.1	0.2	0.1	
Uterus	1.02	10.6	31.5	2.4	54.7	0.1	0.2	0.2	0.1	0.2	
Bladder	1.04	10.5	9.6	2.6	76.1	0.2	0.2	0.2	0.3	0.3	

Table 4. Organ Radiopharmaceutical absorption percentage for 18F-FDG.

Organ/Tissue	Radiopharmaceutical absorption percentage for ^{18}F-FDG
Brain	6%
Heart	3%
Lung	1%
Bladder	6%
Kidney	1.5%
Gonads	1%

In each cycle, the radioactive source is positioned over each organ to measure the dose contribution resulting from the uptake of the radionuclide within the organ and the scattered radiation absorbed by neighboring organs.

2.4 Absorbed Dose Calculation

To estimate the absorbed dose (D) in each organ, the Tally F6 was utilized. The code was compiled for a total of 1×10^8 stories. The following formula was employed for the calculation:

$$D = \sum_{i=1}^{n} Tally_{F6i} * N_i * 1.6x10^{-10} \quad (2)$$

Here, the term "Tally F6i" represents the dose contribution in a specific organ's overall movements of the radioactive source, "Ni" denotes the number of photons emitted by the organ, and $1.6x10^8$ is the conversion factor from MeV/g to J/kg.

3 Results and Discussion.

As previously mentioned, Figure 1 illustrates the phantom shells, while Figure 2 depicts the arrangement of organs within the shell. Utilizing simple geometries aids in reducing the computational time required for calculating the absorbed dose.

To validate the results of the simulation and the proposed model, comparisons were made with those reported by various research groups. Due to the diversity of acquisition protocols and the varying amounts of radiopharmaceuticals injected, individual comparisons were made between each reported result and the phantom proposed in this study. It is noteworthy that different methodologies were employed to estimate the absorbed dose among the reported results, with some authors utilizing phantoms while others reported measurements generated by the PET equipment console.

The results of the absorbed dose in various organs of interest for three different activities: 6.6 mCi, 11 mCi, and 13 mCi, was determined, and compared with those reported by different research groups, except for 6.6 mCi where no reported values were found (refer to Table 5).

Table 5. Absorbed dose with a 6.6 mCi injected activity.

Organ/Tissue	Current study (mGy)
Brain	14.34
Heart	14.97
Eye lens	2.02
Gonads	4.93
Lung	4.08
Kidney	3.01
Thyroid	1.15
Uterus	4.20
Bladder	24.62

Quinn et al.[11] conducted a retrospective study where the absorbed dose in pediatric patients was determined using PET/CT equipment and the GE Dose Watch software. This software records data such as body surface area, weight, and height of the patients. For an activity of 11 mCi (refer to Table 6), our results align well with those reported by Quinn et al.11 for organs such as the gonads, kidneys, and bladder, while there is an underestimation of the dose in other organs. In the case of an activity of 13 mCi (refer to Table 7), Quinn et al.[11] used coefficients for the OLINDA/EXM phantom series that fit the patient profile. Our results for 13 mCi correspond quite well with those reported by Quinn et al.[11] for organs such as the heart, kidneys, gonads, and uterus. However, there is less agreement for the other organs. It is important to note that Quinn et al.[11] did not estimate the absorbed dose in the eye lens in that study.

Table 6: Absorbed dose comparison with an 11 mCi injected activity.

Organ	Current study (mGy)	Quinn et al.[11] (mGy)
Brain	23.90	14.00
Heart	24.95	42.00
Eye lens	3.37	5.50
Gonads	6.17	6.50
Lung	8.31	10.00
Kidney	5.01	5.60
Thyroid	1.92	5.50
Uterus	7.00	10.00
Bladder	41.03	46.00

Table 7: Absorbed dose comparison with a 13 mCi injected activity.

Organ	Current study (mGy)	Quinn et al.[11] (mGy)
Brain	26.07	17.3 ± 3.2
Heart	27.22	29.1 ± 6.2

Eye lens	3.98	---
Gonads	6.73	7.0 ± 1.2
Lung	7.25	10.0 ± 1.8
Kidney	5.92	5.3 ± 0.9
Thyroid	2.09	4.4 ± 0.8
Uterus	7.64	8.8 ± 1.4
Bladder	44.76	79.5 ± 6.7

Once the results of the proposed model had been compared to other studies employing different techniques and methods, the S-values for this phantom were calculated (see Table 8) and compared to the values published by the ICRP24 and Mejia et al.[23] The S-values for the heart, lungs, and uterus using the proposed phantom and methodology are relatively close to those published by the ICRP[24], while the bladder S-value is closer to that published by Mejia et al.[23] However, the S-values for the brain and gonads were significantly different. The gonads present a higher S-value, which could suggest that they are more susceptible to photon absorption than previously thought. For the brain, a reparameterization of the model may be necessary to correct the S-value calculated.

Table 8: S-value comparison .

Organ/Tissue	S-value (mGy/MBq)		
	Current study	ICRP[24]	Mejía et al.[23]
Heart	6.13×10^{-2}	6.50×10^{-2}	4.30×10^{-2}
Lung	1.48×10^{-2}	1.10×10^{-2}	9.40×10^{-3}
Kidney	1.23×10^{-2}	2.10×10^{-2}	2.60×10^{-2}
Bladder	1.01×10^{-1}	1.70×10^{-2}	9.10×10^{-2}
Gonads	2.02×10^{-2}	1.50×10^{-2}	1.30×10^{-2}
Uterus	1.72×10^{-2}	1.50×10^{-2}	1.20×10^{-2}
Brain	5.87×10^{-2}	2.60×10^{-2}	2.80×10^{-2}
Thyroid	4.71×10^{-3}	Not reported	Not reported
Eye lens	8.27×10^{-3}	Not reported	Not reported

Limitations of the Model

The proposed model and phantom do not incorporate the dynamic nature of the circulatory system, thus assuming that the radiopharmaceutical is already distributed within the organs without considering its perfusion process.

Furthermore, several limitations exist within the model. Firstly, the placement of 18F-FDG at the mass center of the organ as a point-like source does not account for its potential absorption throughout the entire volume of the organ. Additionally, the utilization of simple geometries fails to accurately represent the complex shapes of real organs.

Moreover, the time factor in the disintegration process is not considered. It is assumed that 98% of the radiopharmaceutical will have undergone radioactive decay or been eliminated from the body within 10 hours, neglecting the dynamic nature of decay and biological half-life.

4 Conclusions

TThe construction of a pediatric phantom tailored to the characteristics of the proposed Latin American patient profile was successful, particularly given the population's differences in size and weight compared to the European standard. Dosimetry measurements often pose challenges in scalability. Despite the simplicity of the proposed geometry and the omission of dynamic aspects such as the time for the radiopharmaceutical to distribute to various organs, the proposed phantom model closely aligns with values reported in the literature.

An important aspect of the proposed model was the consideration of the source term as isotropic. However, future research should explore the effect of placing different point sources within the organ's delimited volume. For this study, the source was placed solely at the center of mass, without accounting for the radiopharmaceutical distribution throughout the organ.

The model presented in this study offers several advantages over voxelized phantoms and other computational techniques. It does not demand high computational power or time, and its anthropometric features can be easily tailored to any population. The method's simplicity also makes it accessible for implementation in various medical facilities. This marks the development of the first pediatric phantom with anthropometric values specific to the Mexican population, designed for use in pediatric oncology. Despite limitations in the modeling and parameterization process, the efficiency of this type of phantom has been demonstrated. The results obtained can offer guidance for hospitals lagging in the adoption of new technologies and innovation to ensure and promote a culture of radiological safety.

The next step involves applying this methodology to different groups of pediatric patients, as changes in absorbed dose need to be assessed across various ages. Additionally, this methodology can be extended to different radioactive sources such as Cs-137 for cervical cancer or I-131 for thyroid cancer.

To our knowledge, this is one of the few pediatric phantoms incorporating anthropometric values specific to the Latin American population, intended for use in pediatric oncology. Further research will involve replicating this methodology for different groups of pediatric patients, as it is crucial to evaluate variations across different age groups within the field of pediatric oncology. Similarly, this methodology can be adapted for various radioactive sources such as Cs-137 for cervical cancer or I-131 for thyroid cancer.

References

[1] World Health Organization, "Cancer in Children," Who.int, Dec. 13, 2021. https://www.who.int/news-room/fact-sheets/detail/cancer-in-children

[2] J. Zhang et al., "Germline Mutations in Predisposition Genes in Pediatric Cancer," New England Journal of Medicine, vol. 373, no. 24, pp. 2336–2346, Dec. 2015, doi: https://doi.org/10.1056/nejmoa1508054.

[3] P. Vassallo, D. Azzolina, N. Soriani, D. Gregori, and G. Lorenzoni, "Association between simple anthropometric measures in children of different ethnicities: results from the OBEY-AD study," Archivos Latinoamericanos de Nutrición, vol. 67, no. 1, pp. 98–106, Mar. 2017, Accessed: Mar. 27, 2024. [Online]. Available: https://ve.scielo.org/scielo.php?pid=S0004-06222017000100011&script=sci_arttext&tlng=en

[4] A. Pérez Herrera, "Situación actual de la obesidad infantil en méxico," Nutrición Hospitalaria, vol. 36, no. 2, Jan. 2020, doi: https://doi.org/10.20960/nh.2116.

[5] E. Y. Han, W. E. Bolch, and K. F. Eckerman, "REVISIONS TO THE ORNL SERIES OF ADULT AND PEDIATRIC COMPUTATIONAL PHANTOMS FOR USE WITH THE MIRD SCHEMA," Health Physics, vol. 90, no. 4, pp. 337–356, Apr. 2006, doi: https://doi.org/10.1097/01.hp.0000192318.13190.c4.

[6] S. Elmtalab, A. H. Karimi, F. S. K. Mehr, H. Zamani, I. Abedi, and F. Pashaei, "Estimating Radiotherapy-Induced Secondary Cancer Risk Arising from Brain Irradiation at High Energy: A Monte Carlo Study," Frontiers in Biomedical Technologies, vol. 9, no. 1, pp. 53–58, 2022, doi: https://doi.org/10.18502/fbt.v9i1.8145.

[7] D. Krstić and D. Nikezić, "Input files with ORNL—mathematical phantoms of the human body for MCNP-4B," Computer Physics Communications, vol. 176, no. 1, pp. 33–37, Jan. 2007, doi: https://doi.org/10.1016/j.cpc.2006.06.016.

[8] E. Setiawati, Y. Pratama, and M. Azam, "Application of MCNP for determining the distribution of absorbed dose in lung brachytherapy by using radiation γ 131cs," Journal of Physics: Conference Series, vol. 1217, no. 1, pp. 012021–012021, May 2019, doi: https://doi.org/10.1088/1742-6596/1217/1/012021.

[9] J. Valentin, "Radiation dose to patients from

radiopharmaceuticals: (Addendum 2 to ICRP Publication 53) ICRP Publication 80 Approved by the Commission in September 1997," Annals of the ICRP, vol. 28, no. 3, pp. 1–1, Sep. 1998, doi: https://doi.org/10.1016/s0146-6453(99)00006-8.

[10] M. Alkhorayef, "Effective radiation doses in pediatric PET/CT examinations: Pilot study," Applied Radiation and Isotopes, vol. 168, p. 109412, Feb. 2021, doi: https://doi.org/10.1016/j.apradiso.2020.109412.

[11] B. M. Quinn et al., "Patient-adapted organ absorbed dose and effective dose estimates in pediatric 18F-FDG positron emission tomography/computed tomography studies," BMC Medical Imaging, vol. 20, no. 1, Jan. 2020, doi: https://doi.org/10.1186/s12880-020-0415-4.

[12] N. Mohammadi and P. Akhlaghi, "Evaluation of radiation dose to pediatric models from whole body PET/CT imaging," Journal of Applied Clinical Medical Physics, vol. 23, no. 4, p. e13545, Apr. 2022, doi: https://doi.org/10.1002/acm2.13545.

[13] Rosalío Ávila Chaurand, L. R. Prado, and E. L. González, Dimensiones antropométricas de población latinoamericana. Universidad de Guadalajara, Centro Universitario de Arte, Arquitectura y Diseño, División de Tecnología y Procesos, Departamento de Producción y Desarrollo, Centro de Investigaciones en Ergonomía, 2001, 2001.

[14] Coca Perez MA, Efecto de las radiaciones sobre los seres humanos. Organismo Internacional de Energía Atómica (in Spanish), https://humanhealth.iaea.org/hhw/nuclearmedicine/radionuclide_therapy/iaeatrainingcourseandmeetings/regionaltrainingcoursenicaragua2012/efectosbiologicos_macoca.pdf, 2012.

[15] S. Huang et al., "Patient-Specific Dosimetry Using Pretherapy [124I]m-iodobenzylguanidine ([124I]mIBG) Dynamic PET/CT Imaging Before [131I]mIBG Targeted Radionuclide Therapy for Neuroblastoma," Molecular Imaging and Biology, vol. 17, no. 2, pp. 284–294, Aug. 2014, doi: https://doi.org/10.1007/s11307-014-0783-7.

[16] S. Huang, J. Liu, J. Yao, R. Summers, Y. Seo, and C. Lee, "Internal Dosimetry Comparison between Computational Voxelized Human Phantoms and Patient-Specific CT images," Journal of Nuclear Medicine, vol. 56, no. supplement 3, pp. 106–106, May 2015, Accessed: Mar. 27, 2024. [Online]. Available: https://jnm.snmjournals.org/content/56/supplement_3/106.short

[17] M. J. Gelfand, "Dosimetry of FDG PET/CT and other molecular imaging applications in pediatric patients," Pediatric Radiology, vol. 39, no. S1, pp. 46–56, Feb. 2009, doi: https://doi.org/10.1007/s00247-008-1023-6.

[18] C. Lee et al., "Organ and effective doses in pediatric patients undergoing helical multislice computed tomography examination," Medical Physics, vol. 34, no. 5, pp. 1858–1873, Apr. 2007, doi: https://doi.org/10.1118/1.2723885.

[19] "The Radiology Assistant : Normal Values in Ultrasound," radiologyassistant.nl. https://radiologyassistant.nl/pediatrics/normal-values/normal-values-ultrasound

[20] J. C. Bedoya Tobon, "Cálculos dosimétricos mediante código Monte Carlo a partir de imágenes PET/CT .," ricabib.cab.cnea.gov.ar, Dec. 01, 2011. https://ricabib.cab.cnea.gov.ar/305/ (accessed Mar. 27, 2024).

[21] H. Akkurt and K. F. Eckerman, "Development of PIMAL: Mathematical Phantom with Moving Arms and Legs," www.osti.gov, May 01, 2007. https://www.osti.gov/biblio/1339944 (accessed Mar. 27, 2024).

[22] K. Shibuya et al., "Limit of Spatial Resolution in FDG-PET due to Annihilation Photon Non-Collinearity," World Congress on Medical Physics and Biomedical Engineering 2006, vol. 14, pp. 1667–1671, doi: https://doi.org/10.1007/978-3-540-36841-0_411.

[23] A. Mejia, T. Nakamura, I. Masatoshi, J. Hatazawa, M. Masaki, and S. Watanuki, "Measurements of [18F]FDG Activity in Humans â€¢ Mejia et al Estimation of Absorbed Doses in Humans Due to Intravenous Administration of Fluorine-18- Fluorodeoxyglucose in PET Studies," 1990. Accessed: Mar. 27, 2024. [Online]. Available: https://jnm.snmjournals.org/content/jnumed/32/4/699.full.pdf

[24] S. Mattsson et al., "ICRP Publication 128: Radiation Dose to Patients from Radiopharmaceuticals: a Compendium of Current Information Related to Frequently Used Substances," Annals of the ICRP, vol. 44, no. 2_suppl, pp. 7–321, Jun. 2015, doi: https://doi.org/10.1177/0146645314558019.